Carbohydrate Polymers 348 (2025) 122812

Contents lists available at ScienceDirect

Carbohydrate Polymers

journal homepage: www.elsevier.com/locate/carbpol

Influence of TEMPO on preparation of softwood nanofibrils and their hydrogel network properties

Yağmur Baş [a], Linn Berglund [a,*], Jasna S. Stevanic [b], Gerhard Scheepers [c], Totte Niittylä [d], Kristiina Oksman [a,e]

[a] Department of Engineering Sciences and Mathematics, Materials Science, Wood and Bionanocomposites, Luleå University of Technology, 971 87 Luleå, Sweden
[b] RISE Research Institutes of Sweden, Bioeconomy and Health, Sustainable Materials and Packaging, 114 86 Stockholm, Sweden
[c] RISE Research Institutes of Sweden, Built Environment Division, 352 22 Växjö, Sweden
[d] Umeå Plant Science Centre, Department of Forest Genetics and Plant Physiology, Swedish University of Agricultural Sciences, 901 83 Umeå, Sweden
[e] Department of Mechanical & Industrial Engineering (MIE), University of Toronto, Toronto, ON M5S 3G8, Canada

ARTICLE INFO

Keywords:
Cellulose nanofibrils
Wood
TEMPO-oxidation
Hydrogel network
Absorption

ABSTRACT

From an economic and environmental perspective, the use of less chemicals in the production of cellulose nanofibrils (CNFs) is advantageous. In this study, we investigated the oxidation (TEMPO/$NaClO_2$/NaClO, pH 6.8) of softwood (SW) particles with varying amounts of TEMPO (16, 8 or 0 mg g^{-1} of wood). Following, TEMPO-oxidized SW nanofibrils (TO-SWNFs) were obtained by nanofibrillation and their size, morphology, and crystallite size were assessed. Hydrogel networks of TO-SWNFs were prepared and mechanical properties were measured in dH_2O and phosphate buffered saline (PBS) to compare their performance for possible biomedical applications such as wound dressings. The results reveal that the presence of TEMPO is of importance for TO-SWNF network properties, presenting higher eq. H_2O absorption (≈2500 %) and elongation at break (≈10 %) with good wet strength (≈180 kPa). In addition, a decrease in use of TEMPO catalyst from 16 to 8 mg g^{-1} of wood is possible, without detrimental effects on hydrogel network properties (dH_2O absorption ≈ 2000 %, elongation at break ≈ 13 %, wet strength ≈ 190 kPa) related to applications as wound dressings.

1. Introduction

Cellulose, the world's most abundant natural polymer, is a renewable and biodegradable resource (Heinze, 2015) that can be separated into nanofibrils, referred to CNFs having diameters smaller than 100 nm with few μm lengths (Klemm et al., 2011). The regioselective oxidation of primary alcohol groups on cellulose by TEMPO mediated oxidation is a widely used treatment to obtain anionically charged fibers (Isogai, And, & Kato, 1998). The introduction of charge can ease fibrillation by electrostatic repulsion of cellulose chains, improve cross-linking of CNFs via ionic interactions (Cortez-Ruiz et al., 2024), and allow cellulose modification. Such characteristics of TEMPO-oxidized cellulose nanofibrils (TO-CNFs) have led to their use in production of CNF films (Fujisawa, Okita, Fukuzumi, Saito, & Isogai, 2011), hydrogels, and aerogels (Tang et al., 2019). TO-CNFs are studied for various applications such as electronics (Taira et al., 2019), drug delivery (Zong et al., 2022) and hydrogel wound dressings (Baş et al., 2023; Berglund et al., 2023).

TEMPO-oxidation has traditionally been applied on a range of wood celluloses obtained after different pulping processes, such as Kraft (Hou, Chitbanyong, Takeuchi, Shibata, & Isogai, 2023), sulfite (Saito, Nishiyama, Putaux, Vignon, & Isogai, 2006) and thermomechanical pulp (TMP) (Okita, Saito, & Isogai, 2009). As alternative to TEMPO-oxidation of celluloses, we have previously studied the direct TEMPO-oxidation (TEMPO/$NaClO_2$/NaClO, pH 6.8) of wood with variations in the amount of sodium chlorite ($NaClO_2$) and duration of treatment (Jonasson et al., 2021; Jonasson, Bünder, Das, Niittylä, & Oksman, 2021; Jonasson, Bünder, Niittylä, & Oksman, 2020), which allowed the simultaneous delignification and oxidation of hardwood. In a more recent study, we reported on direct TEMPO-oxidation of commercial softwood (SW) particles and their nanofibril networks (Baş et al., 2023). SW particles could potentially be available from sawmills or other wood industries and would therefore be a readily available, low-cost raw material to produce CNFs using a straightforward route. The prepared

* Corresponding author.
E-mail addresses: yagmur.bas@ltu.se (Y. Baş), linn.berglund@ltu.se (L. Berglund), jasna.stevanic@ri.se (J.S. Stevanic), gerhard.scheepers@ri.se (G. Scheepers), totte.niittyla@slu.se (T. Niittylä), kristiina.oksman@ltu.se (K. Oksman).

https://doi.org/10.1016/j.carbpol.2024.122812
Received 26 June 2024; Received in revised form 22 August 2024; Accepted 26 September 2024
Available online 29 September 2024

TO-SWNFs were non-cytotoxic in contact with human fibroblast and keratinocytes, and their networks were shown to have potential as advanced wound dressings performing transparency, high H_2O absorption (≫2500 wt%), and wet tensile strength (≫0.2 MPa) (Baş et al., 2023).

So far, the direct mild (pH 6.8) TEMPO-oxidation on wood was only performed using a method traditionally applied on celluloses (Saito et al., 2009), but with an increase in the amount of primary oxidant $NaClO_2$ considering the simultaneous delignification of wood and oxidation of cellulose. In these studies, (Baş et al., 2023; Berglund et al., 2023; Jonasson et al., 2020; Jonasson, Bünder, Berglund, et al., 2021; Jonasson, Bünder, Das, et al., 2021), a method formerly applied on TMP (Saito et al., 2009) was followed and 16 mg TEMPO g^{-1} dry wood was used. TEMPO is a costly free radical which serves as catalyst in oxidation of primary alcohols, and research is conducted on its negative environmental impact (Mołoń, Szlachcikowska, Stępień, Kielar, & Galiniak, 2023), especially for cases where TEMPO recyclability is not an option concerning nanocellulose quality (Xu, Sanchez-Salvador, Blanco, Balea, & Negro, 2023). In addition, the potential use of TO-CNFs as wound dressings also requires the minimum use and complete removal of TEMPO.

In TEMPO-oxidation of SW TMP (pH 10), delignification of TMP and oxidation of cellulose occur concurrently where the degree of oxidation is related to the amount of NaClO and duration of treatment (Okita et al., 2009). It is also known that carboxyl groups can be produced during bleaching of wood even in absence of TEMPO, with $NaClO_2$ predominantly attacking phenolic lignin rings (Sjöström, 1993). Bragd et al. also discussed possibility of TEMPO free oxidation of cellulose via converting aldehydes to carboxylates, solely utilizing $NaClO_2$ and NaClO (Bragd, van Bekkum, & Besemer, 2004). Similarly, such oxidation might partly occur during TEMPO-mediated oxidation of SW celluloses at a pH of 6.8 (Tanaka, Saito, & Isogai, 2012). In addition, TEMPO-mediated oxidation of TMPs is shown to proceed more efficient in terms of delignification rate in comparison to TEMPO free ones (Ma, Fu, Zhai, Law, & Daneault, 2012). In TMP, wood chips are subjected to pressurized steam, and fibers are produced by breaking up the primary cell wall (Smook, 1999), thus differentiating it from native wood. We hypothesize that the availability of cellulose in native wood structure will change upon variations in amount of TEMPO when wood is used as raw material, thus affect the corresponding fibril and network properties. The amount of TEMPO for oxidation of SW could furthermore be decreased compared to our previous study (Baş et al., 2023), meanwhile still providing nanofibrils with characteristics and network properties for functional hydrogels.

The purpose of this study was to investigate the relationship between TEMPO-oxidation of SW particles and the amount of TEMPO with respect to their nanofibril and hydrogel network properties. Herein, SW was oxidized with varying amounts of TEMPO (16 and 8 mg g^{-1} wood) and constant amounts of $NaClO_2$/NaClO and an identical treatment without TEMPO was also performed to measure the properties of consequent nanofibrils and their hydrogel networks. In connection with our previous works (Baş et al., 2023; Berglund et al., 2023), we focused on assessing the performance of TO-SWNF hydrogel networks obtained for potential as wound dressings, i.e. for applications where they would be in contact with liquids. Characterizations were made focusing on TO-SWNF hydrogel networks, focusing on absorption and retention profiles (dH_2O and PBS) and mechanical properties in wet state.

2. Experimental

2.1. Materials

SW particles (BK 40–90, average size 1–2 mm, mainly spruce-but not exclusively) were purchased from J. Rettenmaier & Söhne GMBH (Rosenberg, Germany). TEMPO, sodium hypochlorite (NaClO), sodium chlorite ($NaClO_2$), sodium phosphate dibasic (Na_2HPO_4), sodium hydroxide (NaOH) and phosphate buffered saline (PBS) and Durapore® membranes were bought from Sigma-Aldrich (Merck Life Sciences AB, Solna, Sweden). Sodium phosphate monobasic (NaH_2PO_4) was bought from G-Biosciences (St. Louis, MO, USA).

2.2. Methods

Fig. 1 shows schematic of the production of SW nanofibril networks using oxidative treatments with variations in TEMPO.

2.2.1. TEMPO-oxidation of SW

For the TEMPO-oxidation, SW particles were directly subjected to a TEMPO/$NaClO_2$/NaClO system in phosphate buffer at pH 6.8 following a previous method, (Baş et al., 2023), but with variations in amount of TEMPO. Briefly, SW particles (5 g, dry weight) were immersed in 500 mL sodium phosphate buffer (pH 6.8) and stirred at RT overnight. Following, TEMPO (8 or 16 mg g^{-1} of wood) and $NaClO_2$ (5 g per g of wood) were added to the buffer and stirred in an oil bath at 60 °C for 1 h. NaClO (2 M, 6–14 %, 10 mL) was added, the flask was stoppered and stirred for a total of 72 h at 60 °C. In addition, an identical oxidation without TEMPO catalyst was performed, where only $NaClO_2$ and NaClO with exact same amounts and procedure were applied. For all treatments, the buffer media was discarded by the end of 72 h, and the insoluble fractions were washed with a total of 2 L dH_2O. TEMPO-oxidized wood samples were denoted as TO16-SW, TO8-SW, where numbers in the abbreviations indicated the amount of TEMPO used as mg g^{-1} wood. TEMPO free treatment of SW sample was considered as oxidized without TEMPO, and denoted as ZT-SW, abbreviating “zero TEMPO”.

2.2.2. Nanofibrillation

After the washings, the consistency of TO16-SW, TO8-SW and ZT-SW slurries was adjusted to 0.75 wt% and were stirred at RT in container bottles for 24 h prior to fibrillation. TO16-SW, TO8-SW and ZT-SW were nanofibrillated in a high shear processor LM20 Microfluidizer (Microfluidics International Corp., Westwood, MA, USA at 1000 bar for 1 pass at and their nanofibrils were denoted as TO16-SWNF, TO8-SWNF and ZT-SWNF respectively.

2.2.3. Preparation of networks

Nanofibril networks with theoretical grammage of 20 g m^{-2} were prepared following a previous method (Baş et al., 2023) with slight modifications. For each sample, nanofibril suspension with 0.25 wt% consistency was prepared and magnetically stirred at RT for 45 min. The suspension was poured on a PVDF membrane (pore size: 0.1 mm, Merck Life Sciences AB, Solna, Sweden) located in a circular shaped sintered glass funnel (90 mm diameter) connected a vacuum pump VCP80 (VWR International AB, Stockholm, Sweden). The nanofibril suspension was filtered for a total of 6 h at RT and a wet cake was obtained. The wet cake on membrane was located between metal meshes and paper tissues, and cold pressed at RT between two plates under a 5.3 kg weight. After 18 h, the dried network self-peeled from the surface of the membrane.

2.3. Characterizations

2.3.1. Yield

The mass yield of after oxidative treatments of SW with and without TEMPO was obtained using the following Eq. 1:

$$Y\ (\%) = \left(\frac{W_f}{W_i}\right) \times 100 \quad (1)$$

where Y is yield, W_f is the final and W_i is the initial dry weight of oxidized fibers and wood, respectively.

2.3.2. Chemical composition of oxidized SW

Gas chromatography/mass spectroscopy (GC/MS) (7890 A/5975C;

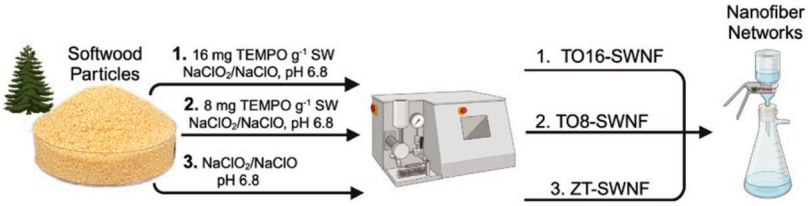

Fig. 1. Process scheme for TEMPO-oxidation of SW particles with variations in TEMPO, mechanical separation step using microfluidization and assembly of nanofibril networks using vacuum filtration.

Agilent Technologies, Santa Clara, CA, USA was used to measure the monosaccharide compositions of amorphous parts of TO16-SW, TO8-SW, ZT-SW and 30 μg of inositol (internal standard), together with standards of nine monosaccharides (Ara, Rha, Fuc, Xyl, Man, Gal, Glc, GalA and GlcA, each at 5, 10, 20, 50 and 100 mg) were methanolyzed using 2 M HCl/methanol followed by trisil reagent (1,1,3,3,3-hexamethyldisilazane + trimethylchlorosilane + pyridine, 3:1:9) and derivatized, and its and derivatised, and its silylated monosaccharides were separated in (Gandla et al., 2015; Gerber, Eliasson, Trygg, Moritz, & Sundberg, 2012; Sweeley, Bentley, Makita, & Wells, 1963). Raw data MS files from GC/MS analysis were converted to NetCDF format in Agilent Chemstation Data Analysis (Version E.02.00.493) and exported to the RDA (version 2016.09; Swedish Metabolomics Centre (SMC), Umeå, Sweden). Data pretreatment procedures, such as baseline correction and chromatogram alignment, peak deconvolution and peak integration followed by peak identification were performed in RDA. 4-*O*-methylglucuronic acid was identified according to a method described (Chong et al., 2013).

The amount of lignin in TO16-SW, TO8-SW, ZT-SW was quantitatively analyzed using based on a protocol previously described (Foster, Martin, & Pauly, 2010). Briefly, lignin was solubilized with acetyl bromide and acetic acid, and solubilized lignin unit aromatic rings were quantified from absorbance values at 280 nm in UV–vis spectrophotometer, where a commercially available Kraft lignin (Sigma-Aldrich 370959) was used as standard to calculate % lignin content (wt/wt) in samples.

2.3.3. Crystallite size

The crystallite size (CS) of the samples was estimated from Wide Angle X-Ray Scattering (WAXS) diffractograms. Measurements were performed on an Anton Paar SAXSpoint 2.0 system (Anton Paar, Gratz, Austria) equipped with a Microsource X-ray source (Cu Ka radiation, wavelength 0.15418 nm) and a Dectris 2D CMOS Eiger R 1 M detector with 75 mm by 75 mm pixel size. All measurements were performed with a beam size of approximately 500 μm diameter, at a sample stage temperature of 25 °C with a beam path pressure at 1–2 mbar. The sample to detector distance (SDD) was 110.6 mm. Dry samples were mounted on a Multi-Solid-Sample Holder, which was further mounted on a Heated Sampler and a VarioStage (Anton Paar, Graz, Austria) and were exposed to vacuum during measurement. For each sample 6 frames of 20 min duration were recorded, giving a total measurement time of 2 h/sample. For all samples the transmittance was determined and used for scaling the scattering intensities. Binning was used to generate graphs with 500 data points, which were used for WAXS diffractograms. The software used for instrument control was SAXSdrive version 2.01.224 (Anton Paar, Graz, Austria), and post-acquisition data processing was performed using the software SAXSanalysis version 3.00.042 (Anton Paar, Graz, Austria). The WAXS diffractograms of the samples were baseline corrected and deconvoluted (i.e., fitted) using Gaussian functions to obtain contributions from cellulose Iβ ($1\bar{1}0$), (110), (102), (200) crystalline planes as well as a non-crystalline contribution. The average crystallite size (CS) was determined according to Scherrer equaton (Eq. 2):

$$CS = \frac{K\,\lambda}{\beta\,\cos\theta} \tag{2}$$

where K is shape factor (0.9), λ is the wavelength of the X-ray radiation (0.15418 nm), β is full width at half height (FWHH) of (200) signal and cos θ is calculated from 2θ that is scattering angle at (200) signal maxima (about 22.5°). WAXS diffractograms were normalized against signal maxima at 16.5°.

2.3.4. Viscoelastic properties

The viscoelastic properties of nanofibril gels (consistency 0.75 wt%) were investigated with a Waters™ TA Instruments Discovery HR20 (TA Instruments, New Castle, DE, USA) using a 25 mm parallel plate geometry. Temperature was controlled at 25 °C with an environmental temperature chamber (ETC). First, the amplitude sweep tests was performed to determine the linear viscoelastic regions (LVER), and the storage (G′) and loss (G″) modulus were measured according to applied shear strain amplitude. Dynamic viscoelastic properties were assessed in frequency sweep tests at 0.1 % strain (in LVER). Steady state viscosity was measured between 0.1 and 100 s^{-1} shear rates.

2.3.5. Carboxylate content

The CC of the oxidized nanofibrils was determined according to a previously described method (Baş et al., 2023). Briefly, 0.1 M hydrochloric acid and 0.01 M sodium chlorite solutions were added to nanofibril (≈0.3 g dry weight) suspensions of TO16-SWNF, TO8-SWNF and ZT-SWNF (125 mL, 0.24 wt%) until the pH of the suspensions was between 2 and 3. An Eco Titrator (Methohm Nordic AB, Bromma, Sweden) was used for conductometric titration with 0.04 M NaOH (addition rate 0.1 mL min^{-1}) until the pH of suspensions has reached 11. Tangent lines were drawn on the titration curve to calculate the volume of NaOH consumed during titration and the carboxylate content was calculated using the following Eq. 3:

$$CC\left(\frac{mmol}{g}\right) = \frac{NaOH\ consumed\ (mL)\ NaOH\ molarity\ (M)}{m\ (g)} \tag{3}$$

where CC is carboxylate content and m is the dry mass of nanofibril sample.

2.3.6. Morphology and nanofibril size distribution

Morphology of the SW fibers before and after fibrillation was observed using polarized optical microscope (POM) and atomic force microscope (AFM). POM images of the materials before and after fibrillation were taken with Nikon Ci Eclipse LV100N POL196 (Nikon, Kanagawa, Japan) with NIS-Elements D 4.30 imaging software at RT and the suspension consistency was 0.5 wt%. For AFM images, 0.005 wt % nanofibril dispersion of TO16-SWNF, TO8-SWNF and ZT-SWNF were drop casted on freshly cleaved mica plates and let dry at ambient conditions for 8 h. Nanofibril morphology was observed using an AFM Veeco Multimode Nanoscope V (Bruker, Santa Barbara, CA, USA) in tapping mode with a silicon cantilever (TESPA-V2, Bruker, spring constant: 42 N m^{-1}). Images were analyzed using Gwyddion software (Necăs & Klapetek, 2012) where mean plane subtraction and horizontal

scar correction were applied. At least a hundred individual nanofibrils were counted from multiple images to plot the nanofibril size distribution profiles of the samples.

2.3.7. Composition of nanofibril networks

The composition of nanofibril networks were studied by Solid-state Cross-Polarization Magic Angle Spinning Carbon-13 Nuclear Magnetic Resonance (CP/MAS ^{13}C NMR) and Fourier-Transform Infrared Spectroscopy (FTIR) spectra. CP/MAS ^{13}C NMR spectra were recorded on water swollen samples packed uniformly in a zirconium oxide (ZrO_2) rotor with a 4 mm outer diameter. CP/MAS ^{13}C NMR spectra were recorded at 295 ± 1 K on a Bruker Avance III AQS 400 SB instrument operating at 9.4 T. The MAS rate was 10 kHz. A 4 mm double air-bearing probe was used. Acquisition was performed with a CP pulse sequence, using a 3.35 μsec proton 90° pulse, 800 μsec ramped (100–50 %) falling contact pulse and a 2.5 s delay between repetitions. A SPINAL64 pulse sequence was used for ^{1}H decoupling. Alpha-glycine (NH_2CH_2COOH) was used for the Hartmann-Hahn matching procedure, as well as an external standard for calibration of the chemical shift scale relative to tetramethylsilane ($(CH_3)_4Si$). The data point of maximum intensity in the alpha-glycine carbonyl (C═O) signal was assigned a chemical shift of 176.03 ppm. 32,768 transitions were recorded on each sample. FTIR spectra of the networks were recorded using a Nicolet Summit Everest with the diamond attenuated total reflectance (ATR, Thermo Fischer Scientific Inc., Waltham, MA, USA). Networks were scanned between 400 and 4000 cm^{-1} wavenumbers at 4 cm^{-1} resolution.

2.3.8. Liquid absorption and retention capacity

For the absorption profiles, networks were immersed completely in dH_2O or PBS medias at RT. At determined time intervals, absorbed networks were weighed after removing the excess liquid on surfaces by gently tapping the samples on a semi-wet tissue. The absorption capacity was calculated according to Eq. 4:

$$\text{Absorption}\ (\%) = \frac{W_t - W_i}{W_i} \times 100 \quad (4)$$

where W_i denotes the initial weight of the dry networks and W_t stands for the weight measured at time t after letting the sample absorb in selected media. For the retention profiles networks were immersed completely in dH_2O or PBS media let 24 h at RT to reach the maximum absorption points. At determined time intervals, networks were weighed to calculate the retention capacities according to the following Eq. 5:

$$\text{Retention}\ (\%) = \frac{W_t}{W_i} \times 100 \quad (5)$$

where W_t denotes the weight of the sample at measurement time t, and W_i stands for the initial weight of the sample at maximum absorption at selected media.

2.3.9. Mechanical properties

The tensile test of the hydrogel networks at equilibrium dH_2O and PBS absorption was performed using a Shimadzu AG-X universal testing machine (Schimadzu Crop., Kyoto, Japan), operating in tensile mode at RT (22.5 °C) equipped with a 1 kN load cell. Strip-shaped samples were cut from networks using a punch with the width of 5.9 mm and length of 80 mm. The samples were conditioned in dH_2O or PBS for 24 h until equilibrium absorption was reached. For the testing, only the center portion of the samples were soaked in the media, and the portion held by the clamps of the tester were let dry. The surplus liquid on the surface of the samples were lightly blotted and the thickness (0.36–0.38 mm for TO16-SWNF and TO8-SWNF, 0.19–0.21 mm for ZT-SWNF networks) was gently measured in between two glass slides using a caliper. The tests were performed at a speed of 20 mm min^{-1} and the gauge length and pre-test force were 50 mm and 0.05 N, respectively. The maximum load at break was recorded to calculate the ultimate tensile strength and elastic modulus was calculated from the slope of the linear elastic region. The elongation was measured from the change of the grip distance divided by gauge length. For each set of networks, at least 4 samples were tested, and the average values were reported with standard deviations.

2.3.10. Light transmittance measurements

The light transmittance measurements on networks were performed between 400 and 800 nm wavelength using a Cary 5000 spectrophotometer equipped with a double monochromator incorporated with an R928 photomultiplier tube detector for UV–vis region.

2.3.11. Thermal properties

The thermal stability measurement of networks was conducted with a STA 449 F3 Jupiter thermogravimetric analyzer (TGA) (NETZSCH-Gerätebau GmbH Branch Office Scandinavia, Täby, Sweden), performed from 20 °C until 500 °C with a heating rate of 10 °C min^{-1} under Ar atmosphere.

3. Results and discussion

The SW particles consisted of about 44 wt% crystalline cellulose and 23.5 wt% lignin, wherein the remaining mass belonged to amorphous cellulose, hemicelluloses and other non-cellulosics (Baş et al., 2023) Table 1 shows the mass yield and lignin contents of TEMPO-oxidized SW with variations in TEMPO. TO16-SW was lignin free where TO8-SW and ZT-SW consisted of lignin lower than 4 wt%. The yields indicated the decrease in lignin and hemicellulose portions of SW in all treatments, with the highest weight loss in case of TO16-SWNF.

The monosaccharide compositions of the amorphous portions of oxidized samples are presented in Table 2.

For all samples, the main sugars after TEMPO-oxidation were xylose, mannose and glucose, belonging to preserved hemicelluloses of galactoglucomannan and arabinoglucuroxylan (Table 2 and Figure S1). No significant difference in the amorphous sugar constituents of TO16-SW, TO8-SW and ZT-SW was observed, reflecting a similar degradation pattern for hemicelluloses in these treatments, irrespective of TEMPO presence. The glucuronic acid portion amorphous monossacharides TO16-SW (1.2 wt%) was higher than TO8-SW (0.8 wt%) and ZT-SW (0.6 wt%), implying a higher degree of oxidation on its amorphous cellulose parts.

Fig. 2 presents the photographs of samples and hydrogel networks, AFM height scans and nanofibril size distribution profiles. Oxidized wood fibers exhibited a similar appearance regardless of the treatment; however, a more gel-like appearance was visible for TO16-SWNFs and TO8-SWNFs in comparison to ZT-SWNF. From the POM images presented in Fig. S2, nanofibrillation was evident for all samples with disappearance of macrofibers after fibrillation. The AFM images of nanofibrils are presented in Fig. 2a, b, and c together with corresponding nanofibril size distribution profiles. The individual nanofibrils were randomly deposited on mica surface and were in nanoscale (width < 100 nm) with average heights of 2.6 ± 1.0 (TO16-SWNF), 2.4 ± 0.8 (TO8-SWNF) and 2.7 ± 1.1 nm (ZT-SWNF) which supported a portion of all samples could be nanofibrillated, however the micrographs represent only the nanofibril fractions. TO16-SWNFs and TO8-SWNFs exhibited

Table 1
Mass yield and lignin content of TEMPO-oxidized SW samples after treatments with varying amounts of TEMPO.

Sample	Yield (%)	Lignin* (wt%)
TO16-SW	36.9 ± 1.5	0.1 ± 0.3
TO8-SW	43.0 ± 6.0	3.8 ± 4.5
ZT-SW	44.1 ± 4.1	1.9 ± 2.7

* The high standard deviations are due to inhomogeneity of lignin presence in sample replicates.

Table 2
Monosaccharide compositions of the 2 M HCl/methanol extracted oxidized SW samples.

Monosugar	TO16-SW (wt%)	TO8-SW (wt%)	ZT-SW (wt%)
Glucose	50.6 ± 0.4	45.1 ± 1.2	51.9 ± 0.4
Mannose	34.3 ± 0.4	35.3 ± 1.3	33.2 ± 0.4
Xylose	11.6 ± 0.4	14.9 ± 0.2	12.1 ± 0.4
Glucuronic acid*	1.2 ± 0.1	0.8 ± 0.1	0.6 ± 0.1
Others	2.3 ± 0.2	3.9 ± 0.5	2.2 ± 0.2

* GC spectra is presented in Fig. S1.

characteristic morphology associated to TO-CNFs, depicting the less ordered crystalline segments located discreetly within nanofibrils, resulting in a "kinked" form (Saito, Kimura, Nishiyama, & Isogai, 2007; Usov et al., 2015). The respective carboxylate content of the nanofibrils were measured as 0.46 ± 0.05, 0.45 ± 0.05 and 0.31 ± 0.01 mmol g^{-1} for TO16-SWNFs, TO8-SWNFs and ZT-SWNFs. The hydrogel networks exhibited high transparency when absorbed in dH_2O as shown in Fig. 2a″, b″ and c″.

Fig. 3 presents the crystallite size (CS) calculated from WAXS measurements of nanofibril networks and their diffractograms. The calculated CS were comparable for TO16-SWNFs and TO8-SWNFs with 3.6 ± 0.1 and 3.7 ± 0.1 nm and were smaller than of ZT-SWNFs with 4.1 ± 0.1 (Fig. 3a). The difference between average nanofibril size measured from AFM height images and calculated CS from WAXS ((200) crystalline plane) might have risen due to the spatiality of microscopy in comparison to bulk sample. The WAXS diffractograms of all samples showed signals with signal maxima appearing at 15°, 16°, 20° and 22.5° attributed to cellulose allomorph I_β structure (Kaffashsaie et al., 2021).

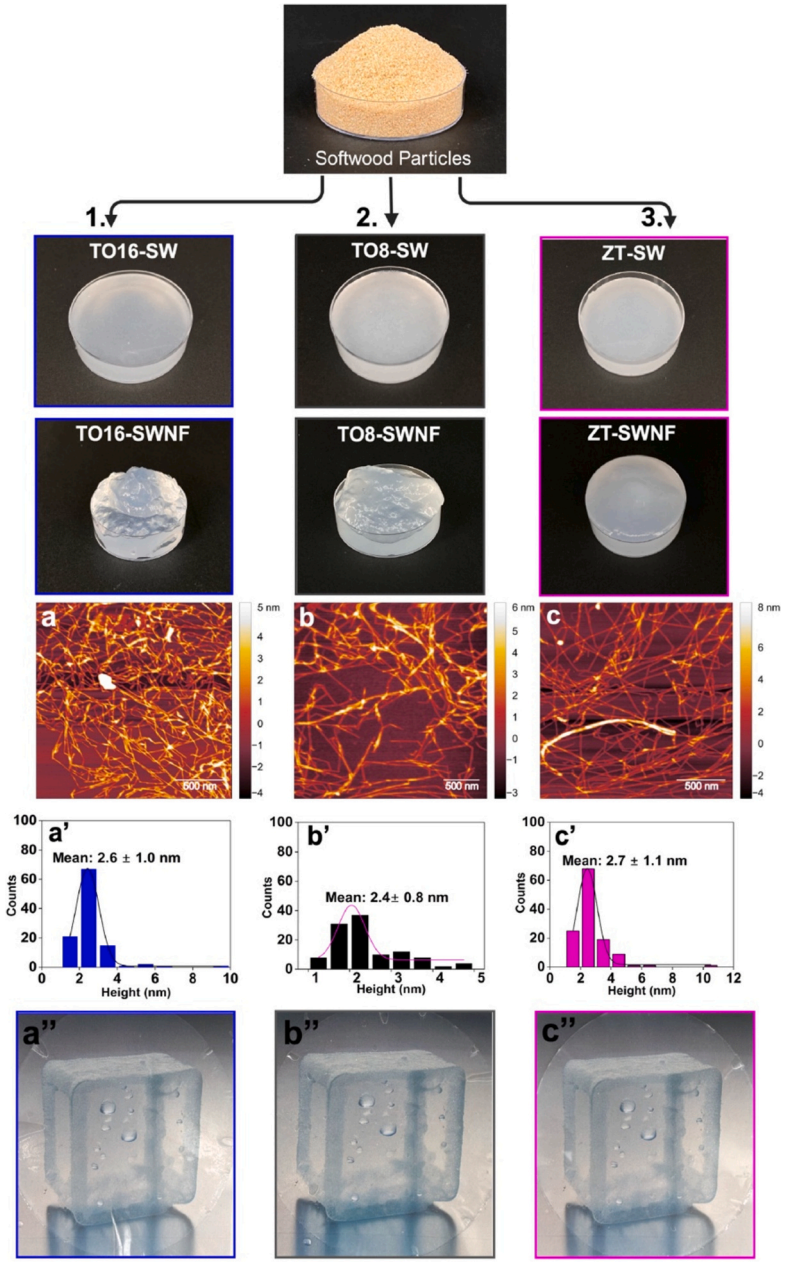

Fig. 2. Photographs of SW particles followed by photographs of oxidized materials using three different treatment routes 1) TO16-SW, 2) TO8-SW and 3) ZT-SW before (row above) and after fibrillation (row below). AFM height images of a) TO16-SWNFs, b) TO8-SWNFs, c) ZT-SWNFs and corresponding nanofibril height distribution profiles of a′) TO16-SWNFs, b′) TO8-SWNFs and c′) ZT-SWNFs. Photographs of a″) TO16-SWNF, b″) TO8-SWNF and c″) ZT-SWNF hydrogel networks absorbed in H_2O.

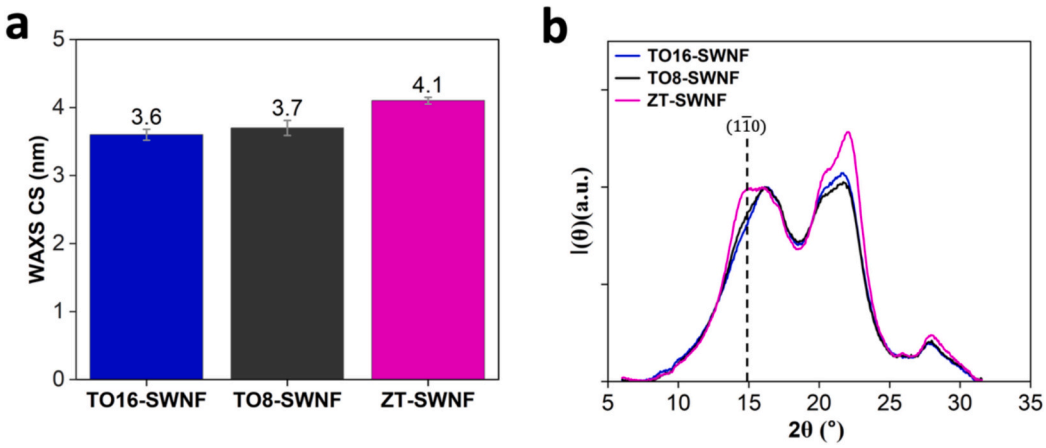

Fig. 3. a) WAXS crystallite size of nanofibril networks and b) WAXS diffractograms of nanofibril networks representing the crystalline properties of nanofibrils.

Rosén et al. showed that the degree of crystallinity of TO-CNF decreased with increased degree of oxidation using WAXD with discussions on fiber surface chains being more disordered (Rosén et al., 2020). Su et al. studied the delamination along the (1$\bar{1}$0) plane of TO-CNFs via following the decrease in (1$\bar{1}$0) reflection signal intensity on WAXS for TEMPO-oxidized spruce celluloses (Su, Burger, Ma, Chu, & Hsiao, 2015). A similar trend was followed in our study for TEMPO-oxidized SW nanofibrils for signal at $2\theta \approx 15°$, hinting the change on fibril surface in relation to TEMPO-oxidation (Fig. 3b). Although a CC of 0.31 ± 0.01 mmol g^{-1} was measured for ZT-SWNFs, the change in (1$\bar{1}$0) plane signal was not as significant for TO16-SWNFs and TO8-SWNFs, implying a contribution mainly from oxidized amorphous cellulose.

Fig. 4 depicts the CP/MAS ^{13}C NMR spectra of TEMPO-oxidized nanofibril networks and SW particles. In TEMPO-oxidation, accessible fibril surfaces can be chemically modified and cause spectral changes in CP/MAS ^{13}C NMR signals of neighboring unmodified surface carbons (Coseri et al., 2015). Using signal fitting in Fig. S3a, the decrease of signal at 84.3 ppm assigned to C4 atoms of surface polymers belonging to the fibril phase boundary parallel to the (1$\bar{1}$0) plane was followed (Fig. S4) (Rosén et al., 2020).

From Fig. 4, the lignin signal at 56 ppm in SW spectra disappeared for all nanofibril networks indicating delignification. From NMR it was possible to follow the change of C6 (66 ppm) crystalline signal area to surface C6 (63 ppm) signals, suggesting the difference upon treatments of C6 in different samples (Su et al., 2015). A new signal around 94 ppm attributed to C1 reducing ends due to break of 1,4-glycosidic bonds was observed for TEMPO-oxidized delignified wood (Su et al., 2015), and was not observed in any of the spectra in this study, which might indicate the preservation of cellulose chains of directly treated SW samples.

Fig. 5 shows the rheology measurements of nanofibril gels at 0.75 wt % consistency. All nanofibril samples displayed similar G′ and G″ regardless of presence of TEMPO in the treatment (Fig. 5a). Increased surface charge enhances the repulsion between fibrils during fibrillation under shear, resulting in reduced inter-fibril friction with fewer aggregations and yields lower viscosities (Geng et al., 2018; Liao, Pham, & Breedveld, 2020). A relation between the viscosity and aspect ratio in

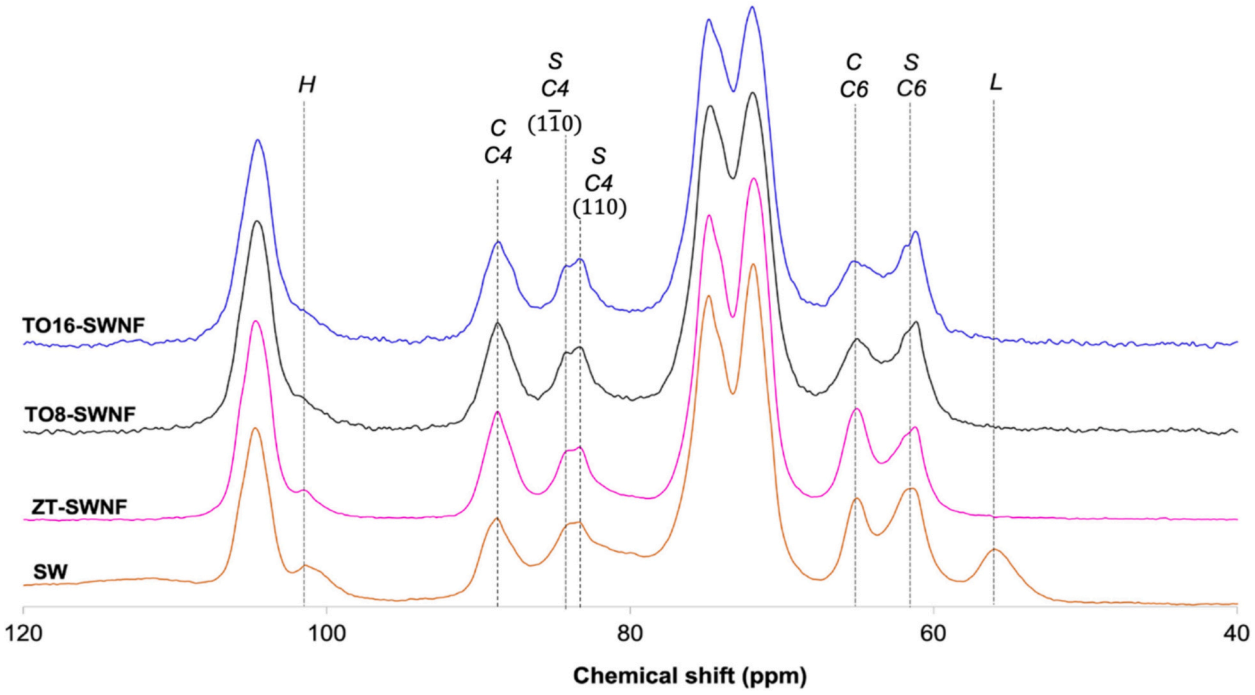

Fig. 4. CP/MAS ^{13}C NMR spectra showing the composition of nanofibril networks and SW. Signal assignments denotes: C: crystalline, S: surface, H: hemicellulose, L: lignin.

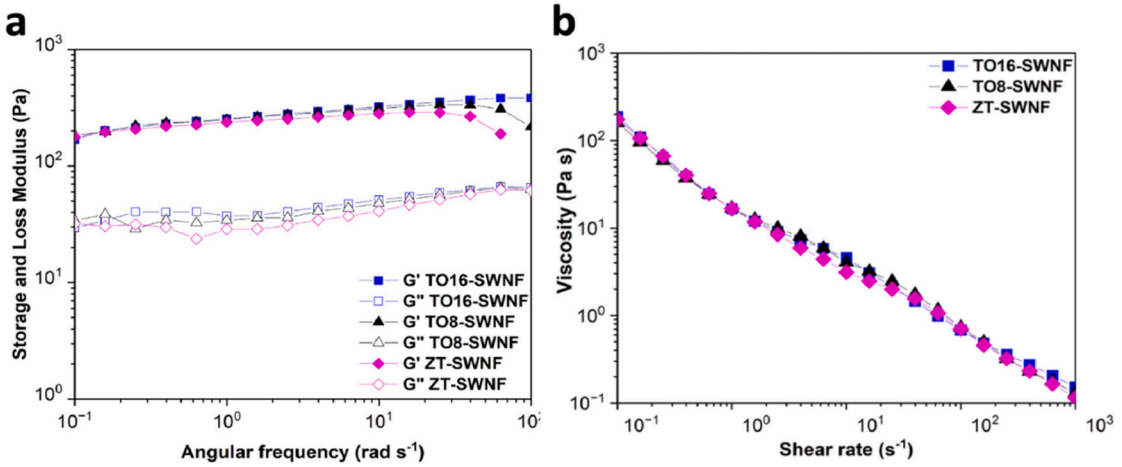

Fig. 5. Viscoelastic properties of the nanofibril gels assessed in: a) Frequency sweep test showing storage (G′) and loss (G″) modulus upon change in angular frequency and b) flow sweep test with change in complex viscosity upon increasing applied shear rate.

association with onset of percolation was studied for TO-CNF samples with similar carboxylate contents (Moberg et al., 2017). Herein, the similar viscosity values for TO16-SWNF and TO8-SWNF in comparison to ZT-SWNF might have resulted from a contribution of a higher aspect ratio of nanofibrils when TEMPO was present in treatments. Nanofibrils exhibited similar viscosities within applied shear rates (Fig. 4b), that were an order of magnitude greater than the viscosity of TO-CNFs with 1.1 mmol g^{-1} CC and 0.72 wt% consistency (Liao, Pham, & Breedveld, 2021). All samples showed the characteristic shear-thinning behavior of CNFs within the applied shear rates (Fig. 5b).

Fig. 6 shows UV–Vis transmittance, FTIR spectra, TGA and DTG profiles of networks. Transparency allows monitoring wound care process while unnecessary dressing replacement is avoided (Kuddushi, Shah, Ayranci, & Zhang, 2023), therefore assessing transparency is relevant for advanced dressings. The UV–Visible spectra of nanofibril networks are shown in Fig. 6a, where the highest transmittance was exhibited for TO16-SWNF (≈38–32 %) network, followed by TO8-SWNF (≈34–28 %) and ZT-SWNF (≈31–24 %) networks. The higher transmittance of TO16-SWNF suggests a larger portion of nanofibrils present after fibrillation in comparison to TO8-SWNF and ZT-SWNF. All hydrogel networks were highly transparent in water absorbed state (Fig. 2).

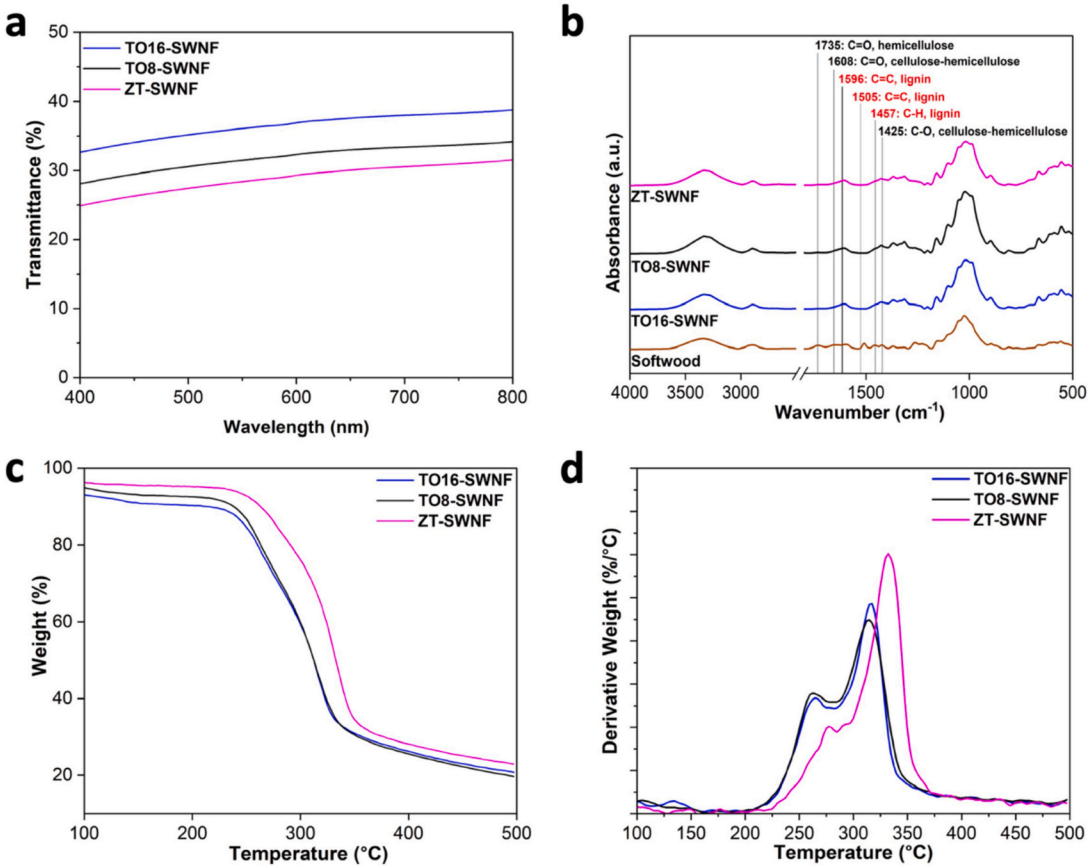

Fig. 6. a) UV–Visible transmittance spectra, b) FTIR spectra, c) TGA and d) DTG of the nanofibril networks.

Fig. 6b depicts the FTIR spectra of the nanofibril networks and SW particles. A signal belonging C═O stretching vibrations of sodium carboxylate at 1608 cm^{-1} can be detected for all networks but not for SW particles, accompanied with a signal at 1425 cm^{-1}, attributed to C—O stretching of carboxylates of oxidized cellulose (da Silva Perez, Montanari, & Vignon, 2003; Kaffashsaie et al., 2021). The signal at 1735 cm^{-1} assigned to C═O stretching band of hemicellulose carboxylic acids was prominent for SW particles, and its intensity decreased in nanofibril network spectra (Fig. S5). Signals at 1596 and 1505 (C═C, aromatic rings), 1457 cm^{-1} (C—H deformations) and 1264 cm^{-1} (C—O stretching, guiacyl linkage) (Pandey & Pitman, 2003) belonging to lignin are present for SW, and absent for the networks, regarding delignification that was also supported via chemical composition analysis and CP/MAS ^{13}C NMR (Fig. 3 and Table 1).

Fig. 6c shows the weight loss profile of the networks in TGA, where the slight loss before 200 °C is due to removal of absorbed moisture. The TGA profiles of TO16-SWNF and TO8-SWNF did not show a significant difference, however their thermal decomposition temperatures were lower than ZT-SWNF due to a higher number of anhydroglucuronic acid units present on TEMPO-oxidized wood nanofibrils that were decarbonized in heating (Fukuzumi, Saito, Okita, & Isogai, 2010). A visible shift in the DTG peaks of ZT-SWNF from 277 °C to 262C° and 332 °C to 317 °C could be observed in Fig. 5d, due to the forementioned effect of a higher number of anhydroglucuronic acids present in TO16-SWNF and TO8-SWNF. The DTG peaks showed two key characteristics for all networks: the T_d belonging to the degradation of sodium anhydroglucuronate units (277C° for ZT-SWNF and 262 °C for TO16-SWNF and TO8-SWNF) and crystalline cellulose, but with a decrease in its T_d due to the presence of thermally unstable anhydroglucuronates (332C° for ZT-SWNF and 317 °C for TO16-SWNF and TO8-SWNF). (Fukuzumi et al., 2010) A smaller signal as a shoulder at 292 °C could also be seen from the DTG profile of ZT-SWNF network.

The absorption and retention capacity of CNF networks are pertinent where excess wound exudates and toxic compounds need to be removed while humidity at wound-dressing interface is sustained (Lloyd, Kennedy, Methacanon, Paterson, & Knill, 1998). TO16-SWNF and TO8-SWNF networks immediately absorbed water upon contact (Video, Supplementary). The osmolarity and ionic concentration of PBS buffer can resemble an environment like human body fluids, and assessment in dH_2O and PBS might be reflective on performance upon applications of networks as wound dressings. Fig. 7a and b shows the absorption and Fig. 7c and d retention profiles of the networks in dH_2O and PBS media, respectively.

The equilibrium dH_2O absorption for TO16-SWNF, TO8-SWNF and ZT-SWNF was 2387 ± 45, 1900 ± 56 %, 1104 ± 45 %, respectively (Fig. 7a). TO16-SWNF and TO8-SWNF networks have reached equilibrium dH_2O absorption at around 5 h whereas ZT-SWNF networks, it took <3 h. This was attributed to the higher CC of TO16-SWNF and TO8-SWNF networks. For all networks, the absorption values in PBS at 24 h were similar with 891 ± 95 % (TO16-SWNF), 904 ± 58 % (TO8-SWNF) and 854 ± 106 % (ZT-SWNF) and were lower than their dH_2O absorption values (Fig. 7b). In addition, the difference in maximum absorption of networks in PBS was not as trivial when compared to their dH_2O absorption profiles, where possible interactions of anionic charges on oxidized wood nanofibrils and the electrolytes of PBS might have lowered the absorption on the nanofibrillar surfaces (Tehrani, Nordli, Pukstad, Gethin, & Chinga-Carrasco, 2016).

At 30 min, TO16-SWNF (54 %), TO8-SWNF (64 %) and ZT-SWNF

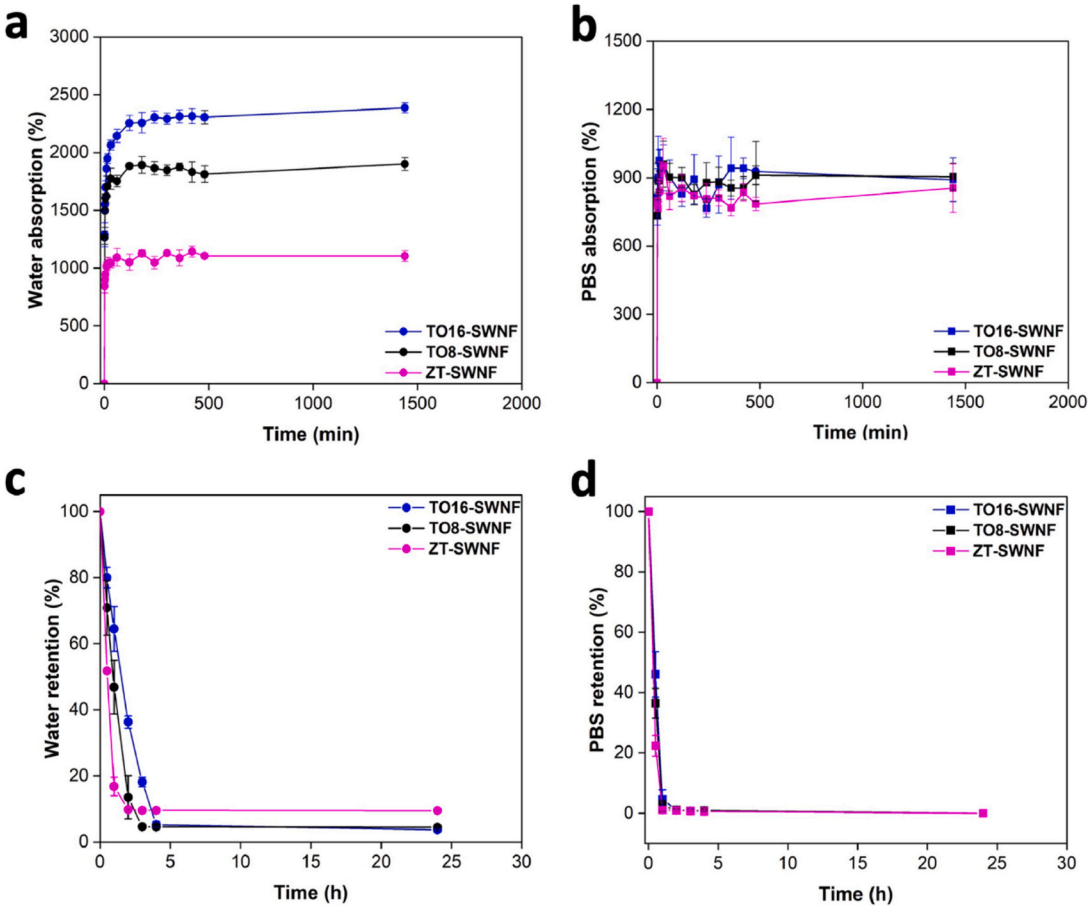

Fig. 7. Absorption profiles of the networks in a) dH_2O, b) PBS and retention profiles of networks in c) dH_2O and d) PBS. TO16-SWNF networks exhibited the highest absorption in both dH_2O and PBS, while no significant differences for retention profiles for networks when absorbed in PBS.

(78 %), lost different percentage of their initial equilibrium absorbed dH_2O weights with a higher retention ability for TO16-SWNF (Fig. 7c and Fig. S6a). For all networks, the retention in PBS was stabilized by the end of 2 h without a distinct difference in profiles (Fig. 7d and S6b).

For the potential applications of networks as wound dressings, the evaluation of mechanical performance at wet conditions is of interest, as such materials must maintain their structural integrity with appropriate strength and extensibility, while matching the elastic properties of the skin to avoid decohesion at dressing edges when applied on patients (Sun, Nordli, Pukstad, Kristofer Gamstedt, & Chinga-Carrasco, 2017). Therefore, we evaluated the mechanical properties of hydrogel networks in equilibrium absorption in dH_2O and PBS, as presented with representative stress-strain curves in Fig. 8 with a summary of properties given in Tables S1 and S2. For all materials, networks in PBS showed higher ultimate tensile strength (UTS) and elongation at break than in dH_2O. Herein, the low UTS upon absorption of dH_2O or PBS can be explained by strength lowering effect of dH_2O molecules in networks by weakening the interfibrillar interactions (Haslach, 2009). The UTS of hydrogel networks at equilibrium dH_2O absorption were between 180 and 240 kPa with elongation at break of 4–13 % (Fig. 8a). TO16-SWNF and TO8-SWNF hydrogel networks had a lower UTS compared to the ZT-SWNF ones, which was due to their higher dH_2O content (Table S1). ZT-SWNF hydrogel networks showed the smallest elongation at break in dH_2O (Fig. 8a and Table S1), which likely was related to their lower degree of fibrillation. The higher flexibility of TO16-SWNF and TO8-SWNF hydrogel networks is beneficial from a wound management perspective as it increases the conformability of the dressings (Queen, Evans, Gaylor, & Courtney, 1987).

The UTS at equilibrium PBS absorption were between 0.6 and 2.3 MPa, with TO16-SWNF network having the largest UTS (Fig. 8b and Table S2). As a result of the lower absorption in PBS, interfibrillar interactions were disrupted less, and the UTS of networks in PBS was higher than their UTS at H_2O. The elongation at break for hydrogel networks at equilibrium PBS absorption was between 6 and 13 %, with higher ductility for all networks in comparison to when absorbed in dH_2O.

In dH_2O, the moduli of TO16-SWNF and TO8-SWNF networks were found relatively lower (7–8 MPa) in comparison to their moduli in PBS (Tables S1, S2), which fall within the limits of reported modulus of human skin measured in tensile tests (Agache, Monneur, Leveque, & De Rigal, 1980). The higher modulus of ZT-SWNF hydrogel network in comparison to others in dH_2O is attributed to its lower absorption, and thus less dH_2O present in the network. Interestingly, TO8-SWNF and ZT-SWNF hydrogel networks exhibited similar modulus when absorbed in PBS, which were lower than the modulus of TO16-SWNF hydrogel networks (Fig. 8b and Table S2). In addition, the modulus of ZT-SWNF in PBS was found slightly lower than its modulus in dH_2O (Tables S1 and S2), although the absorption in dH_2O was higher than PBS (Fig. 7a and b). The modulus trend was not the same for the networks in dH_2O and PBS, and the main reason for difference in modulus was considered as variations in degree of fibrillation and absorption behaviors. In addition, when absorbed in PBS, a contribution of carboxylate content to modulus was likely, as TO16-SWNF and TO8-SWNF networks composed of nanofibrils with higher carboxylate content than ZT-SWNF networks, also exhibited higher modulus. However, this cannot explain the wet mechanical behavior alone since the measured carboxylate content is not significantly different for TO16-SWNFs and TO8-SWNFs, while a difference in their modulus was clear. Supposedly, the interactions between the anionic sites of oxidized nanofibrils and electrolytes present in PBS might have contributed to the increased moduli via moderating repulsion between the anions, while lowering swelling on fibril surfaces (Tehrani et al., 2016). The elastic modulus of human skin is reported between 0.1 and 20 MPa range with large variations and values depending highly on the measuring technique i.e. torsion, indentation or tensile tests, and tissue length scale (Agache et al., 1980; Pailler-Mattei, Bec, & Zahouani, 2008; Wahlsten et al., 2023). Similar viscoelastic response was found in dH_2O for TO16-SWNF and TO8-SWNF networks with G' values higher than that of ZT-SWNF networks during relaxation stages after sequential compressions with 1 N and 4 N (Fig. S7). The results presented in this study denoted the potential applications of hydrogel networks as wound dressings, where TO16-SWNF and TO8-SWNF networks exhibited more relevant properties considering the extensibility both in dH_2O and PBS together with higher absorption abilities.

4. Conclusions

This study provides an insight on the influence of TEMPO within the context of direct TEMPO-oxidation of commercially available SW particles (TEMPO/$NaClO_2$/NaClO, pH 6.8) regarding to its presence and amount in oxidation media. The presence of TEMPO was positive for absorption and mechanical properties of corresponding hydrogel networks in comparison to TEMPO free oxidation and a decrease in the amount of TEMPO from 16 to 8 mg g^{-1} SW showed minor effect on nanofibril and hydrogel network properties when applied with same amount of $NaClO_2$/NaClO. The change of C4 signal intensities in solid-state CP/MAS ^{13}C NMR suggested fibril delamination via TEMPO-oxidation, and WAXS validated the change on $(11\bar{0})$ plane of SW nanofibrils in direct TEMPO treatments. The TO16-SWNF and TO8-SWNF hydrogel networks in dH_2O exhibited similar tensile strength

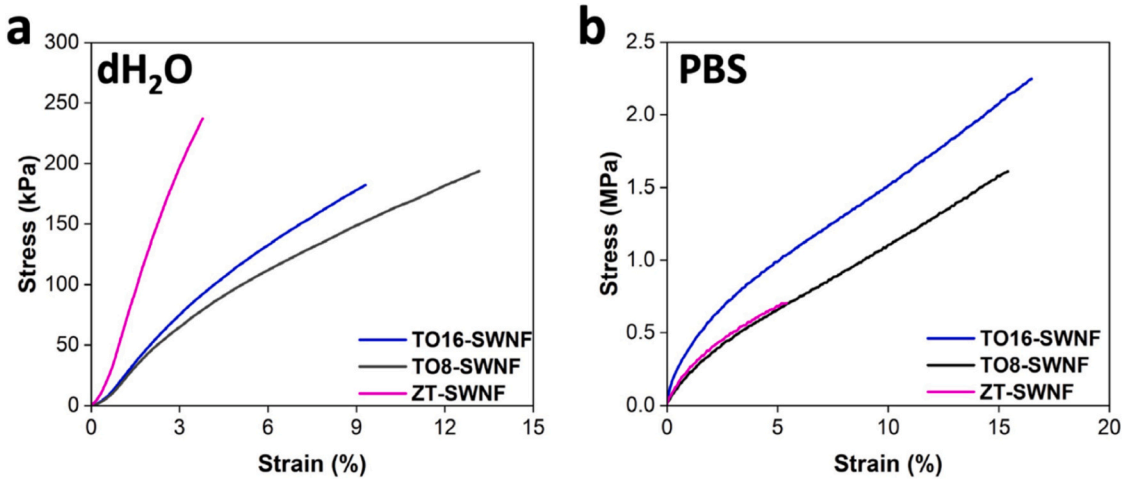

Fig. 8. Representative stress-strain curves showing the mechanical properties of hydrogel networks at 24 h a) dH_2O and b) PBS absorption.

(≈0.18 MPa, ≈0.19 MPa, respectively), elongation at break (≈9 %, ≈13 %, respectively) and modulus (≈8 MPa, ≈7 MPa, respectively). A trend in relation to carboxylate content and degree of fibrillation was observed in H_2O absorption of nanofibril networks, while different treatments had minor effects on absorption in PBS. Amount of absorbed H_2O in networks governed the wet mechanical properties to an extent with moderating the UTS with increased extensibility. A decrease in use of TEMPO from 16 mg to 8 mg g^{-1} wood was shown to be possible without affecting the network performance for properties related to applications as wound dressings assessed in this study.

Supplementary data to this article can be found online at https://doi.org/10.1016/j.carbpol.2024.122812.

CRediT authorship contribution statement

Yağmur Baş: Writing – review & editing, Writing – original draft, Visualization, Validation, Methodology, Investigation, Data curation. **Linn Berglund:** Writing – review & editing, Writing – original draft, Supervision, Resources, Funding acquisition, Formal analysis, Conceptualization. **Jasna S. Stevanic:** Writing – review & editing, Writing – original draft, Data curation. **Gerhard Scheepers:** Formal analysis, Resources, Writing – review & editing. **Totte Niittylä:** Writing – review & editing, Resources, Formal analysis. **Kristiina Oksman:** Writing – review & editing, Writing – original draft, Resources, Funding acquisition.

Declaration of competing interest

The authors declare that they have no known competing financial interests or personal relationships that could have appeared to influence the work reported in this paper.

Data availability

Data will be made available on request.

Acknowledgements

This project was funded by the Swedish Foundation for Strategic Research within the HEALiX project [RMX18-0039]. Funding through Stiftelsen Gunnar Sundblads forskningsfond through Young Researcher's Award is acknowledged. The authors are grateful to Junko Takahashi-Schmidt and Sonja Viljamaa at Umeå Plant Science Centre (UPSC) and the Biopolymer Analytical Platform (BAP) at UPSC/SLU supported by Bio4Energy for their help with pyrolysis-GC/MS and acetyl bromide lignin analysis. The authors thank the Swedish Metabolomics Center (SMC) for the RDA software and Jessica Lindén for their contribution in retention experiments. Illustrations were created with BioRender.

References

Agache, P. G., Monneur, C., Leveque, J. L., & De Rigal, J. (1980). Mechanical properties and Young's modulus of human skin in vivo. *Archives of Dermatological Research, 269*, 221–232.

Baş, Y., Berglund, L., Niittylä, T., Zattarin, E., Aili, D., Sotra, Z., … Oksman, K. (2023). Preparation and characterization of softwood and hardwood nanofibril hydrogels: Toward wound dressing applications. *Biomacromolecules, 24*(12), 5605–5619.

Berglund, L., Squinca, P., Baş, Y., Zattarin, E., Aili, D., Rakar, J., … Oksman, K. (2023). Self-assembly of nanocellulose hydrogels mimicking bacterial cellulose for wound dressing applications. *Biomacromolecules, 24*(5), 2264–2277.

Bragd, P. L., van Bekkum, H., & Besemer, A. C. (2004). TEMPO-mediated oxidation of polysaccharides: Survey of methods and applications. *Topics in Catalysis, 27*, 49–66.

Chong, S. L., Koutaniemi, S., Virkki, L., Pynnönen, H., Tuomainen, P., & Tenkanen, M. (2013). Quantitation of 4-O-methylglucuronic acid from plant cell walls. *Carbohydrate Polymers, 91*(2), 626–630.

Cortez-Ruiz, M., Garemark, J., Ritter, M., Brusentsev, Y., Larsson, T., Olsén, P., & Wågberg, L. (2024). Structure-properties relationships of defined CNF single-networks crosslinked by telechelic PEGs. *Carbohydrate Polymers, 339*, Article 122245.

Coseri, S., Biliuta, G., Fras Zemljič, L., Stevanic Srndovic, J., Larsson, P. T., Strnad, S., … Lindström, T. (2015). One-shot carboxylation of microcrystalline cellulose in the presence of nitroxyl radicals and sodium periodate. *RSC Advances, 5*, 96927.

Foster, C. E., Martin, T. M., & Pauly, M. (2010). Comprehensive compositional analysis of plant cell walls (lignocellulosic biomass) part I: Lignin. *Journal of Visualized Experiments, 37*, 1745.

Fujisawa, S., Okita, Y., Fukuzumi, H., Saito, T., & Isogai, A. (2011). Preparation and characterization of TEMPO-oxidized cellulose nanofibril films with free carboxyl groups. *Carbohydrate Polymers, 84*(1), 579–583.

Fukuzumi, H., Saito, T., Okita, Y., & Isogai, A. (2010). Thermal stabilization of TEMPO-oxidized cellulose. *Polymer Degradation and Stability, 95*(9), 1502–1508.

Gandla, M. L., Derba-Maceluch, M., Liu, X., Gerber, L., Master, E. R., Mellerowicz, E. J., & Jönsson, L. J. (2015). Expression of a fungal glucuronoyl esterase in populus: Effects on wood properties and saccharification efficiency. *Phytochemistry, 112*(1), 210–220.

Geng, L., Mittal, N., Zhan, C., Ansari, F., Sharma, P. R., Peng, X., … Söderberg, L. D. (2018). Understanding the mechanistic behavior of highly charged cellulose nanofibers in aqueous systems. *Macromolecules, 51*(4), 1498–1506.

Gerber, L., Eliasson, M., Trygg, J., Moritz, T., & Sundberg, B. (2012). Multivariate curve resolution provides a high-throughput data processing pipeline for pyrolysis-gas-chromatography/mass-spectrometry. *Journal of Applied Pyrolysis, 95*, 95–100.

Haslach, H. W. (2009). The moisture and rate-dependent mechanical properties of paper: A review. *Mechanics of Time-dependent Materials, 4*, 11–35.

Heinze, T. (2015). Cellulose: Structure and properties. In , *Advances in Polymer Science: vol 271. Cellulose chemistry and properties: Fibers, nanocelluloses and advanced materials*. Cham: Springer.

Hou, G., Chitbanyong, K., Takeuchi, M., Shibata, I., & Isogai, A. (2023). Comprehensive study of preparation of carboxy group-containing cellulose fibers from dry-lap kraft pulps by catalytic oxidation with solid NaOCl. *ACS Sustainable Chemistry and Engineering, 11*(40), 14782–14792.

Isogai, A., And, Ã., & Kato, Y. (1998). Preparation of polyuronic acid from cellulose by TEMPO-mediated oxidation. *Cellulose, 5*, 153–164.

Jonasson, S., Bünder, A., Berglund, L., Hertzberg, M., Niittylä, T., & Oksman, K. (2021). The effect of high lignin content on oxidative nanofibrillation of wood cell wall. *Nanomaterials, 11*(5), 1179.

Jonasson, S., Bünder, A., Das, O., Niittylä, T., & Oksman, K. (2021). Comparison of tension wood and normal wood for oxidative nanofibrillation and network characteristics. *Cellulose, 28*(2), 1085–1104.

Jonasson, S., Bünder, A., Niittylä, T., & Oksman, K. (2020). Isolation and characterization of cellulose nanofibers from aspen wood using derivatizing and non-derivatizing pretreatments. *Cellulose, 27*(1), 185–203.

Kaffashsaie, E., Yousefi, H., Nishino, T., Matsumoto, T., Mashkour, M., Madhoushi, M., & Kawaguchi, H. (2021). Direct conversion of raw wood to TEMPO-oxidized cellulose nanofibers. *Carbohydrate Polymers, 262*, Article 117938.

Klemm, D., Kramer, F., Moritz, S., Lindström, T., Ankerfors, M., Gray, D., & Dorris, A. (2011). Nanocelluloses: A new family of nature-based materials. *Angewandte Chemie International Edition, 50*(24), 5438–5466.

Kuddushi, M., Shah, A. A., Ayranci, C., & Zhang, X. (2023). Recent advanced in novel materials and techniques for developing transparent wound dressings. *Journal of Materials Chemistry B, 11*, 6201–6224.

Liao, J., Pham, K. A., & Breedveld, V. (2020). Rheological characterization and modeling of cellulose nanocrystal and TEMPO-oxidized cellulose nanofibril suspensions. *Cellulose, 27*(7), 3741–3757.

Liao, J., Pham, K. A., & Breedveld, V. (2021). TEMPO-CNF suspensions in the viscoelastic regime: Capturing the effect of morphology and surface charge with a rheological parameter. *Cellulose, 28*(2), 813–827.

Lloyd, L. L., Kennedy, J. F., Methacanon, P., Paterson, M., & Knill, C. J. (1998). Carbohydrate polymers as wound management aids. *Carbohydrate Polymers, 37*(3), 315–322.

Ma, P., Fu, S., Zhai, H., Law, K., & Daneault, C. (2012). Influence of TEMPO-mediated oxidation on the lignin of thermomechanical pulp. *Bioresource Technology, 118*, 607–610.

Moberg, T., Sahlin, K., Yao, K., Geng, S., Westman, G., Zhou, Q., … Rigdahl, M. (2017). Rheological properties of nanocellulose suspensions: Effects of fibril/particle dimensions and surface characteristics. *Cellulose, 24*(6), 2499–2510.

Mołoń, M., Szlachcikowska, D., Stępień, K., Kielar, P., & Galiniak, S. (2023). Two faces of TEMPO (2,2,6,6-tetramethylpiperidinyl-1-oxyl) — An antioxidant or a toxin? *Biochimica et Biophysica Acta — Molecular Cell Research, 1870*(2), Article 119412.

Necăs, D., & Klapetek, P. (2012). Gwyddion: An open-source software for SPM data analysis. *Open Physics, 10*(1), 181–188.

Okita, Y., Saito, T., & Isogai, A. (2009). TEMPO-mediated oxidation of softwood thermomechanical pulp. *Holzforschung, 63*(5), 529–535.

Pailler-Mattei, C., Bec, S., & Zahouani, H. (2008). In vivo measurements of the elastic mechanical properties of human skin by indentation tests. *Medical Engineering & Physics, 30*(5), 599–606.

Pandey, K. K., & Pitman, A. J. (2003). FTIR studies of the changes in wood chemistry following decay by brown-rot and white-rot fungi. *International Biodeterioration and Biodegradation, 52*(3), 151–160.

Queen, D., Evans, J. H., Gaylor, J. D. S., & Courtney, J. M. (1987). An *in vitro* assessment of wound dressing conformability. *Biomaterials, 8*, 372–376.

Rosén, T., He, H. R., Wang, R., Zhan, C., Chodankar, S., Fall, A., … Hsiao, B. S. (2020). Cross-sections of nanocellulose from wood analyzed by quantized polydispersity of elementary microfibrils. *ACS Nano, 14*(12), 16743–16754.

Saito, T., Hirota, M., Tamura, N., Kimura, S., Fukuzumi, H., Heux, L., & Isogai, A. (2009). Individualization of nano-sized plant cellulose fibrils by direct surface carboxylation using TEMPO catalyst under neutral conditions. *Biomacromolecules, 10*(7), 1992–1996.

Saito, T., Kimura, S., Nishiyama, Y., & Isogai, A. (2007). Cellulose nanofibers prepared by TEMPO-mediated oxidation of native cellulose. *Biomacromolecules, 8*(8), 2485–2491.
Saito, T., Nishiyama, Y., Putaux, J. L., Vignon, M., & Isogai, A. (2006). Homogeneous suspensions of individualized microfibrils from TEMPO-catalyzed oxidation of native cellulose. *Biomacromolecules, 7*(6), 1687–1691.
da Silva Perez, D., Montanari, S., & Vignon, M. R. (2003). TEMPO-mediated oxidation of cellulose III. *Biomacromolecules, 4*(5), 1417–1425.
Sjöström, E. (1993). *Wood chemistry: Fundamentals and applications* (2nd ed.). Cambridge, MA: Elsevier Academic Press (Chapter 8).
Smook, G. A. (1999). *Handbook for pulp & paper technologists* (4th printing). Vancouver: Angus Wilde Publications Inc. (Chapter 5).
Su, Y., Burger, C., Ma, H., Chu, B., & Hsiao, B. S. (2015). Exploring the nature of cellulose microfibrils. *Biomacromolecules, 16*(4), 1201–1209.
Sun, F., Nordli, H. R., Pukstad, B., Kristofer Gamstedt, E., & Chinga-Carrasco, G. (2017). Mechanical characteristics of nanocellulose-PEG bionanocomposite wound dressings in wet conditions. *Journal of the Mechanical Behavior of Biomedical Materials, 69*, 377–384.
Sweeley, C. C., Bentley, R., Makita, M., & Wells, W. W. (1963). Gas-liquid chromatography of trimethylsilyl derivatives of sugars and related substances. *Journal of the American Chemical Society, 85*(16), 2497–2507.
Taira, S., Kurihara, M., Koda, K., Sugimura, K., Nishio, Y., & Uraki, Y. (2019). TEMPO-oxidized cellulose nanofiber-reinforced lignin based polyester films as a separator for electric double-layer capacitor. *Cellulose, 26*(1), 569–580.
Tanaka, R., Saito, T., & Isogai, A. (2012). Cellulose nanofibrils prepared from softwood cellulose by TEMPO/NaClO/$NaClO_2$ systems in water at pH 4.8 or 6.8. *International Journal of Biological Macromolecules, 51*(3), 228–234.
Tang, J., Song, Y., Zhao, F., Spinney, S., da Silva Bernardes, J., & Tam, K. C. (2019). Compressible cellulose nanofibril (CNF) based aerogels produced via a bio-inspired strategy for heavy metal ion and dye removal. *Carbohydrate Polymers, 208*, 404–412.
Tehrani, Z., Nordli, H. R., Pukstad, B., Gethin, D. T., & Chinga-Carrasco, G. (2016). Translucent and ductile nanocellulose-PEG bionanocomposites—a novel substrate with potential to be functionalized by printing for wound dressing applications. *Industrial Crops and Products, 93*, 193–202.
Usov, I., Nyström, G., Adamcik, J., Handschin, S., Schutz, C., Fall, A., Bergström, L., & Mezzenga, R. (2015). Understanding nanocellulose chirality and structure-properties relationship at the single fibril level. *Nature Communications, 6*, 7564.
Wahlsten, A., Stracuzzi, A., Lüchtefeld, I., Restivo, G., Lindenblatt, N., Giampietro, C., … Mazza, E. (2023). Multiscale mechanical analysis of the elastic modulus of skin. *Acta Biomaterialia, 170*, 155–168.
Xu, H., Sanchez-Salvador, J. L., Blanco, A., Balea, A., & Negro, C. (2023). Recycling of TEMPO-mediated oxidation medium and its effect on nanocellulose properties. *Carbohydrate Polymers, 319*, Article 121168.
Zong, S., Wen, H., Lv, H., Li, T., Tang, R., Liu, L., Jiang, J., Wang, S., & Duan, J. (2022). Intelligent hydrogel with both redox and thermo-response based on cellulose nanofiber for controlled drug delivery. *Carbohydrate Polymers, 278*, Article 118943.